

THE EFFECT OF MIXING ON THE OBSERVED METALLICITY OF THE SMITH CLOUD

DAVID B. HENLEY, JEFFREY A. GRITTON, AND ROBIN L. SHELTON
 Department of Physics and Astronomy, University of Georgia, Athens, GA 30602
 dbh@physast.uga.edu, jgritton@uga.edu, rls@physast.uga.edu

Draft version July 9, 2021

ABSTRACT

Measurements of high-velocity clouds' metallicities provide important clues about their origins, and hence on whether they play a role in fueling ongoing star formation in the Galaxy. However, accurate interpretation of these measurements requires compensating for the galactic material that has been mixed into the clouds. In order to determine how much the metallicity changes as a result of this mixing, we have carried out three-dimensional wind-tunnel-like hydrodynamical simulations of an example cloud. Our model cloud is patterned after the Smith Cloud, a particularly well-studied cloud of mass $\sim 5 \times 10^6 M_\odot$. We calculated the fraction of the high-velocity material that had originated in the galactic halo, F_h , for various sight lines passing through our model cloud. We find that F_h generally increases with distance from the head of the cloud, reaching ~ 0.5 in the tail of the cloud. Models in which the metallicities (relative to solar) of the original cloud, Z_{cl} , and of the halo, Z_h , are in the approximate ranges $0.1 \lesssim Z_{cl} \lesssim 0.3$ and $0.7 \lesssim Z_h \lesssim 1.0$, respectively, are in rough agreement with the observations. Models with $Z_h \sim 0.1$ and $Z_{cl} \gtrsim 0.5$ are also in rough agreement with the observations, but such a low halo metallicity is inconsistent with recent independent measurements. We conclude that the Smith Cloud's observed metallicity may not be a true reflection of its original metallicity and that the cloud's ultimate origin remains uncertain.

Subject headings: Galaxy: halo — hydrodynamics — ISM: clouds — ISM: individual objects (Smith Cloud) — methods: numerical

1. INTRODUCTION

High-velocity clouds (HVCs) are clouds in the Galactic halo traveling at high speed relative to the local standard of rest ($\gtrsim 90 \text{ km s}^{-1}$; Wakker & van Woerden 1997). HVCs play an important role in the Galaxy, by supplying material to fuel star formation. However, their origins are uncertain, with Galactic fountains, gas stripped from satellite galaxies, and remnants from the formation of the Local Group all having been suggested as possible origins (see reviews by Bregman 2004 and Putman et al. 2012). The metallicity of an HVC is key to determining its origin, as it allows us to distinguish between material that has or has not been processed through the Galactic disk.

The Smith Cloud (SC; Smith 1963) is arguably the best-characterized of the Galaxy's HVCs. Its distance and mass are both known: $12.4 \pm 1.3 \text{ kpc}$ (Lockman et al. 2008, hereafter L08) and $\gtrsim 10^6 M_\odot$ each in H I and H II (L08; Hill et al. 2009, hereafter H09; Lockman 2015), respectively. The cloud is located approximately 3 kpc from the Galactic midplane, is approximately $1 \text{ kpc} \times 3 \text{ kpc}$ on the sky, and is thought to be moving in the direction of its major axis. Uniquely among HVCs, its three-dimensional velocity is also constrained. From the variation in the line-of-sight velocity across the cloud, L08 concluded that the cloud is approaching the disk at $\sim 70 \text{ km s}^{-1}$ on a prograde orbit $\sim 50 \text{ km s}^{-1}$ faster than the Galactic rotation. Based purely on its orbit, L08 were unable to favor a Galactic or extragalactic origin for the SC, and pointed out the need to measure its metallicity.

Using measurements of the [N II] emission from the SC's head, H09 determined that the cloud's nitrogen abundance is likely 0.15–0.44 times solar, and concluded

that this low abundance supported the idea that the cloud represents new material that is being accreted onto the Galaxy. On the other hand, using S II absorption lines observed along three sight lines passing through the cloud's tail, Fox et al. (2016, hereafter F16) measured the cloud's sulfur abundance to be $0.53^{+0.21}_{-0.15}$ times solar. Based on this, and the orbit determined by L08, F16 concluded that the SC had a Galactic origin (specifically, in the outer disk $\sim 13 \text{ kpc}$ from Galactic Center, where the metallicity is half solar).

It is important to note that the cloud should have experienced some mixing with the surrounding gas. Using hydrodynamical simulations, Gritton et al. (2014) showed that the high-velocity material in the tail of an HVC may contain significant amounts of material that originated in the halo as a result. Therefore, the true metallicity of the original cloud is not simply given by measurements of the metallicity of the high-velocity material, but depends also on the halo metallicity and the degree of mixing between the halo and the cloud.

The goal of the current study is to determine how extensively mixing has changed the metallicity of an example HVC, the SC. To this end, we present three-dimensional hydrodynamical simulations of an SC-like HVC traveling through the halo (Section 2). We use these simulations to quantify the degree of mixing of cloud and halo material (Section 3), and examine the relationship between the resulting metallicities and H09's and F16's metallicity measurements (Section 4). We discuss our results in Section 5.

TABLE 1
REFERENCE MODEL (MODEL A) PARAMETERS

Quantity	Symbol	Value
Domain x range		-2.56 to $+2.56$ kpc
Domain y range		0 to $+2.56$ kpc
Domain z range		-1.28 to $+14.08$ kpc
Spatial resolution ^{a,b}		10 to 160 pc
Cooling curve metallicity ^c	Z_{cool}	$10^{-0.5} Z_{\odot}$
Cloud radius	r_{cl}	500 pc
Cloud hydrogen density	$n_{\text{H,cl}}$	0.4 cm^{-3}
Cloud temperature ^d	T_{cl}	1500 K
Cloud speed	$ \mathbf{v}_{\text{cl}} $	150 km s^{-1}
Ambient halo temperature	T_{h}	2×10^6 K
Ambient halo hydrogen density ^e	$n_{\text{H,h}}$	$3 \times 10^{-4} \text{ cm}^{-3}$

^a We used adaptive mesh refinement during the simulation. If the whole domain were modeled at full resolution, the grid would consist of $512 \times 256 \times 1536$ cells, each of size $(10 \text{ pc})^3$.

^b In models Alr and Ahr, the maximum resolution was 20 and 5 pc, respectively.

^c In Model B, we used $Z_{\text{cool}} = Z_{\odot}$.

^d Set by requiring pressure balance between the cloud and the ambient medium. In Model C, $T_{\text{cl}} = 2500$ K.

^e In Model C, $n_{\text{H,h}} = 5 \times 10^{-4} \text{ cm}^{-3}$.

2. HYDRODYNAMICAL SIMULATIONS

2.1. Model Description

We used FLASH (Fryxell et al. 2000) version 4.2 to simulate the hydrodynamical interaction between our model cloud and the halo. We used a three-dimensional Cartesian domain. Our simulations are similar to Model B in Gritton et al. (2014), in that the cloud started at rest at the origin, and the ambient medium flowed upward through the domain with velocity $-\mathbf{v}_{\text{cl}} = |\mathbf{v}_{\text{cl}}|\hat{\mathbf{z}}$, where \mathbf{v}_{cl} is the cloud’s velocity in the ISM rest frame. This enabled us to study the cloud’s evolution over a long period of time, without the need for a prohibitively large domain. However, whereas Gritton et al. (2014) modeled a quarter-cloud, assuming symmetry about the $x = 0$ and $y = 0$ planes, here we modeled a half-cloud, assuming symmetry only about the $y = 0$ plane. The size of our model domain is summarized in Table 1, as are the other model parameters and notation, discussed below.

Our reference model is called Model A. Following Galyardt & Shelton (2016), we initialized the cloud as a sphere of radius $r_{\text{cl}} = 500$ pc with hydrogen number density $n_{\text{H,cl}} = 0.4 \text{ cm}^{-3}$ and hydrogen to helium ratio of 10 to 1. Note that, at maximum resolution, the cloud’s diameter is covered by 100 cells (for an example comparison, the corresponding number of cells from Gritton et al. 2014 is 33). The cloud’s density profile follows a hyperbolic tangent function at the cloud edge (Kwak et al. 2011; Gritton et al. 2014). This yields a total hydrogen mass of $5 \times 10^6 M_{\odot}$, similar to the observed mass of the SC (L08; H09). Also, the model cloud’s initial diameter is equal to the observed length of the SC’s minor axis (~ 1 kpc; note that the cloud is thought to be moving in the direction of its major axis; L08). The model cloud’s initial speed relative to the ISM was 150 km s^{-1} (i.e., the ambient medium flowed in the $+z$ direction at 150 km s^{-1}). Although this is slightly higher than the SC’s current speed relative to the ISM ($130 \pm 14 \text{ km s}^{-1}$; L08), the ram pressure of the ISM causes the cloud to

decelerate relative to the ISM during the course of the simulation.

We assumed that the temperature of the ambient halo is $T_{\text{h}} = 2 \times 10^6$ K (e.g., Henley & Shelton 2013, 2015). The density of the halo is uncertain, though various observational constraints imply that it does not exceed a few times 10^{-4} cm^{-3} , except in the lower halo (see, e.g., discussion in Kwak et al. 2011, Section 2 and Henley et al. 2014, Section 4.1). Miller & Bregman (2013) used O VII absorption line measurements to model the halo density. Their best-fit model implies that the halo density at the SC’s current Galactocentric distance (L08) is $6 \times 10^{-4} \text{ cm}^{-3}$. If we follow L08 and use the cloud’s current position and velocity to calculate its past trajectory within the Galactic potential of Wolfire et al. (1995b) (neglecting drag), we find that the cloud would have experienced an ambient density of $\sim (3\text{--}6) \times 10^{-4} \text{ cm}^{-3}$ over the past ~ 60 Myr (cf., on this trajectory, the cloud would have been in the disk ~ 70 Myr ago; L08). For our reference model, we assumed a constant ambient density of $n_{\text{H,h}} = 3 \times 10^{-4} \text{ cm}^{-3}$. The temperature of the cloud (1500 K in Model A) was set by requiring pressure balance between the cloud and the ambient medium.

Radiative cooling depends on the metallicity of the gas, which is uncertain in the SC and in its environment. As the halo’s metallicity is likely to be subsolar, for our reference model we used the Sutherland & Dopita (1993) cooling curve with metallicity $\log(Z_{\text{cool}}/Z_{\odot}) = -0.5$ (relative to the Anders & Grevesse 1989 solar abundances). Note that radiative cooling was suppressed below 10^4 K (i.e., the cooling curve was set to zero below this temperature). This prevents runaway cooling of the coolest, densest gas. The physical justification for such a cut-off is that the cool gas will be heated by the ambient ultraviolet radiation field, by photoemission from dust grains (Wolfire et al. 1995a). However, we did not attempt to model this heating, and we acknowledge that this heating rate will be lower above the disk (where our model cloud resides) than in the disk (Wolfire et al. 1995b). The simulation time step was limited by multiple criteria and

at no time was greater than half of the cooling time in any cell in the model domain.

In order to test the sensitivity of our results to the assumed cooling curve, we tried a model that used a solar-metallicity cooling curve (Model B). To test the sensitivity to the ambient gas density, we tried a variant with $\log(Z_{\text{cool}}/Z_{\odot}) = -0.5$ but a higher ambient density, $n_{\text{H,h}} = 5 \times 10^{-4} \text{ cm}^{-3}$ (Model C).¹ Finally, to test the sensitivity to the simulation resolution, we tried two variants in which the maximum resolution was twice or half that of our reference model (Models Ahr (high resolution) and Alr (low resolution), respectively).

We traced the mixing of cloud and halo material by defining two inert fluids which were advected with the flow, one representing the cloud material and the other the ambient material. The mass fractions of these fluids were initially one and zero, respectively, within the cloud, and vice versa outside the cloud. When postprocessing the simulations, we determined the fraction of the material in each grid cell that originated in the halo, f_{h} , directly from these fluids' mass fractions.

We ran the simulations for 400 Myr. This is several times longer than the time the SC is expected to have spent in the halo, assuming it has stayed on its current trajectory (L08). However, running our simulation for this length of time ensures that the mixing in the model cloud's tail has reached a reasonably steady state (see Section 3). It also allows us to quantify the time variability of that mixing, which we use to estimate the uncertainty in the degree of mixing at the current epoch.

Our simulations do not include a magnetic field or the possibility that the SC may have a dark matter minihalo, both of which would affect the degree of mixing in the tail. It is not clear how significant these omissions are. Nor do our simulations collide the SC with the Galactic disk (Nichols et al. 2014), a scenario that Galyardt & Shelton (2016) found would destroy the cloud even if the SC has a dark matter minihalo.

2.2. Results

Figure 1 shows slices through the reference model domain, showing the density at 100-Myr intervals. The upward-flowing ambient medium ablates material from the cloud, which mixes with the halo gas and gets stretched out in the $+z$ direction. There is considerable spatial and temporal variation in the structure of the tail.

When we compare Model B (Figure 2) with Model A, we find that the Model A cloud fragments more than the Model B cloud. This difference appears to originate in the first ~ 90 Myr of the clouds' evolution. At $t \sim 20$ Myr, a vortex emerges from the back of each cloud, causing the hot ambient medium to be mixed in behind the cloud (Figure 3), forming intermediate-temperature gas. In Model B, starting from $t \sim 60$ Myr, this gas cools and becomes denser than in Model A, because of

¹ We also experimented with a model with $n_{\text{H,h}} = 6 \times 10^{-4} \text{ cm}^{-3}$, which is equal to the halo density at the SC's current location (using the Miller & Bregman 2013 halo model). However, we found that the resulting higher ram pressure of the ambient medium braked the high-velocity material too severely, meaning that there was virtually no high-velocity material at angles $\gtrsim 25^\circ$ behind the cloud head (cf. F16's sight lines lie $14\text{--}28^\circ$ behind the SC head).

Model B's larger cooling rate. This tends to smooth out the density structure behind the cloud, which impairs the fragmentation of the cloud, compared with Model A.

In Model C (Figure 4), the cloud is pushed further up through the model domain than in Model A, because of the greater ram pressure of the ambient medium. (At $t = 400$ Myr, the cloud head is at $z = 6.6$ and 4.1 kpc in Models C and A, respectively.) The Model C cloud also fragments less than the Model A cloud. This result is surprising, as the timescale for the growth of Kelvin-Helmholtz instabilities is expected to be smaller in Model C, due to the smaller density contrast between the cloud and the ambient gas (Chandrasekhar 1961).

3. MIXING OF HALO AND CLOUD MATERIAL

We calculated the proportion of halo material within the high-velocity gas on various sight lines running through our model domain in the following manner. We first defined high-velocity material as that which travels faster than 90 km s^{-1} relative to the ambient medium. We then defined f_{h} for any given cell in the simulational domain as the fraction of the high-velocity material in that cell that originated in the halo. Thus, $1 - f_{\text{h}}$ is the fraction of the high-velocity material in the cell that originated in the HVC. For any sight line through the simulational domain, the fraction of the high-velocity material that originated in the halo is

$$F_{\text{h}} = \frac{\int f_{\text{h}} \rho dl}{\int \rho dl}, \quad (1)$$

where ρ is the gas density and only high-velocity gas is included in the integrals.

We then determined the angle that the simulational domain must be viewed at so as to mimic actual observations of the SC's head and tail. This angle is equal to the angle between the SC's velocity relative to the surrounding co-rotating ISM and the line of sight to the SC's head, which, based on the cloud's position, distance, and velocity from L08, is 130° .

We determined where the cloud's head is located, when viewed from this angle, by choosing the line of sight that has the greatest high-velocity hydrogen column density, $N_{\text{H,HVC}}$, from all of the lines of sight that cross the z axis of our domain at 130° . This was done at every model epoch in order to determine the location of the cloud's head as a function of time.²

We examined a series of sight lines that cross through the z axis of the domain behind the cloud's head. The angles between each of these sight lines and the sight line through the cloud's head were determined from the assumption that the observer was on Earth, 12.4 kpc (L08) from the SC (see Figures 1, 2, and 4). Figure 5(a) shows F_{h} as a function of this angle for Model A at various epochs. For angles $\lesssim 30^\circ$, F_{h} reaches a reasonably steady state by $t = 300$ Myr (i.e., the variation of F_{h} from epoch to epoch is relatively small compared to earlier epochs).

² At some epochs, dense regions would form temporarily in the tail of the model HVC, meaning that the maximum of $N_{\text{H,HVC}}$ was several kiloparsecs behind the front of the model HVC. Therefore, in order to prevent one of these temporary dense regions in the model cloud's tail being defined as the cloud head, we restricted our search for the maximum of $N_{\text{H,HVC}}$ to within 2 kpc of the cloud front.

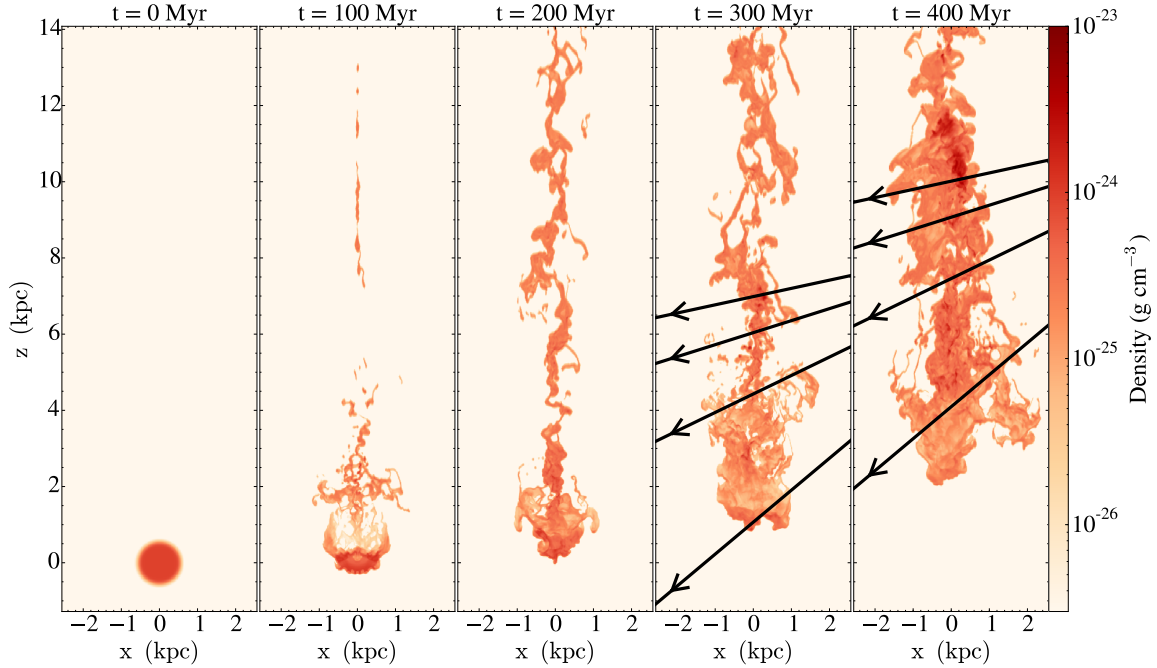


FIG. 1.— Slices through our reference model domain, showing the density in the xz plane at $t = 0, 100, \dots, 400$ Myr (left to right). The diagonal black lines in the later epochs' plots show model sight lines used to calculate the fraction of the high-velocity material that originated in the halo (Section 3). These sight lines are from a vantage point to the right of the model domain, 12.4 kpc from the cloud head, and cross the z axis at angles corresponding to the observational sight lines in Table 2.

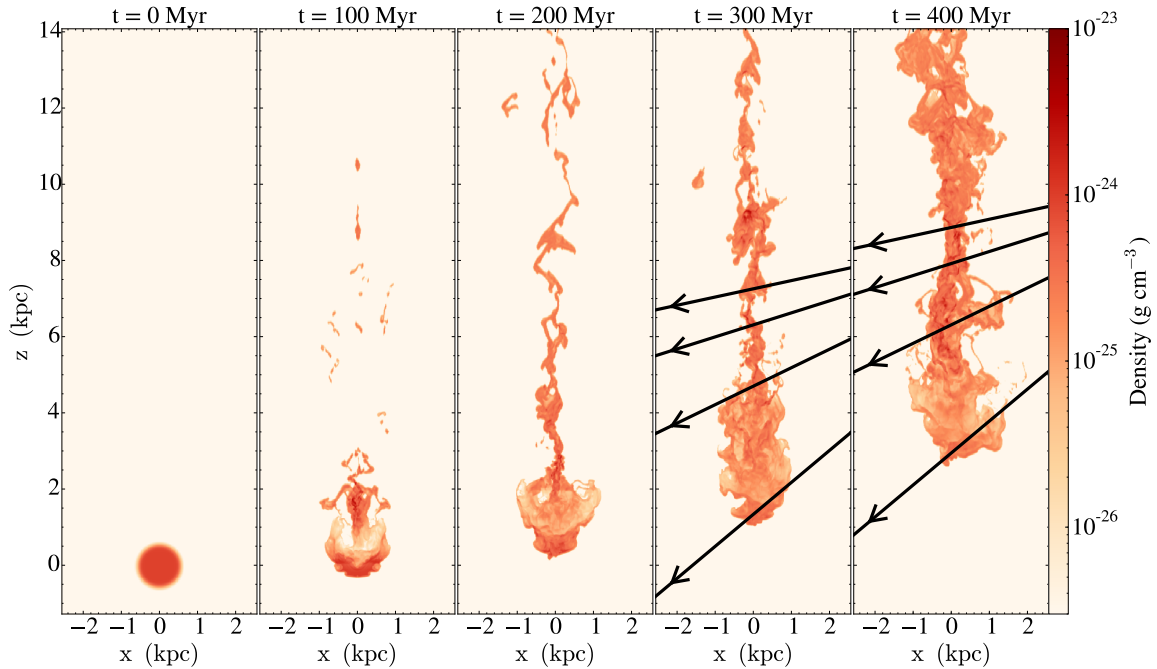


FIG. 2.— Same as Figure 1, but for Model B.

However, there is still some time variation of the F_h profiles due to the fact that the flow in the model HVC's tail is not steady, and for the last few tens of megayears of the simulation, F_h is drifting toward larger values for angles $\lesssim 15^\circ$. For Models B and C (Figures 5(b) and (c), respectively), we find that F_h also reaches a reasonably steady state by around $t = 300$ Myr, although again there is some time variation of the F_h profiles. In addition, the Model C profiles exhibit gaps at some angles, meaning

that there is no material above the high-velocity cut-off along the sight line at those particular angles. These gaps in the high-velocity material distribution are due to the higher-density ambient medium having a stronger braking effect on the cloud material than in the other models (this braking effect was noted in footnote 1 for a model with an even higher ambient density, for which the effect was more severe than in Model C).

Figure 6 shows F_h averaged over multiple epochs.

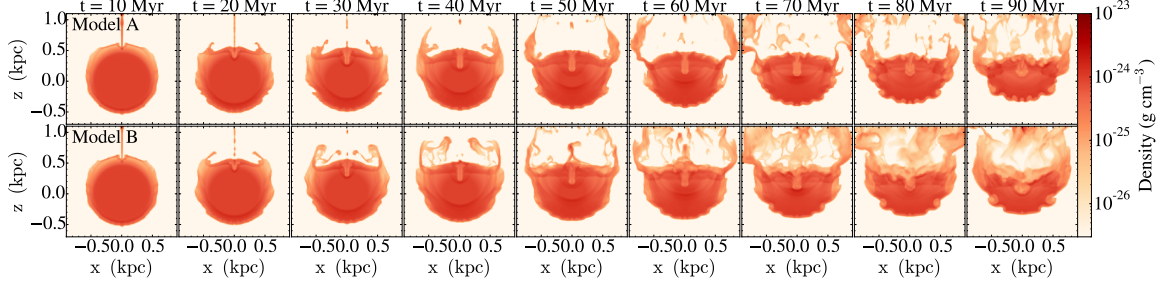


FIG. 3.— Comparison of the densities in the xz plane near the origin from Models A (upper row) and B (lower row), at $t = 10, 20, \dots, 90$ Myr (left to right).

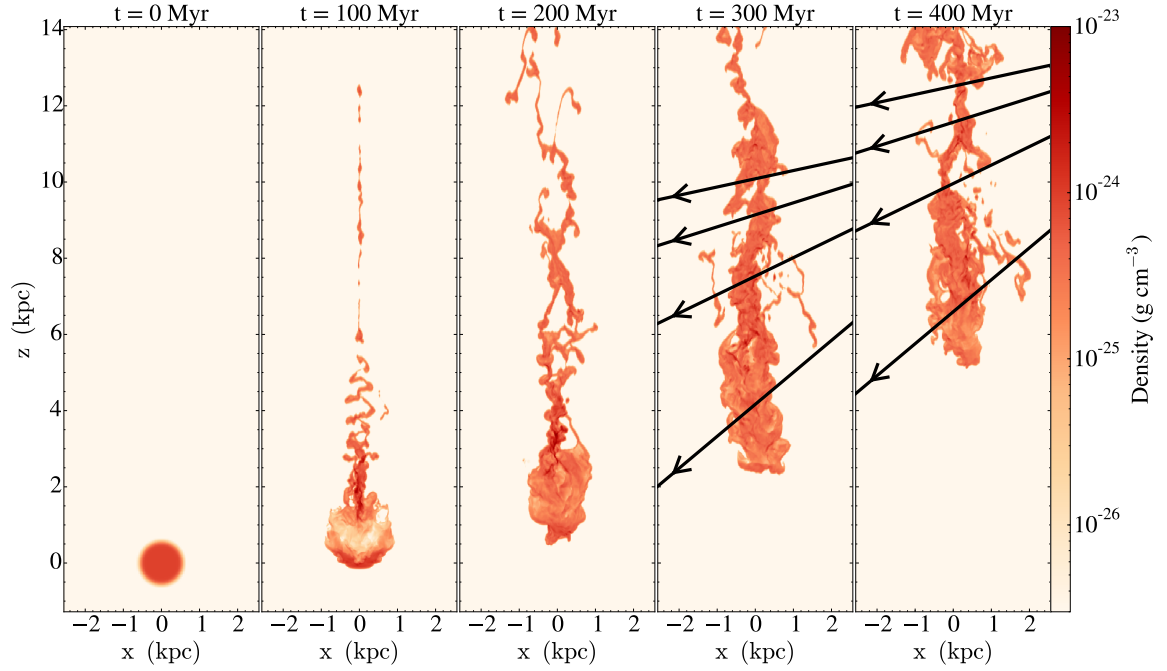


FIG. 4.— Same as Figure 1, but for Model C.

TABLE 2
OBSERVATION DETAILS AND MODEL RESULTS

Target	l (deg)	b (deg)	Dist. from SC head ^a (deg)	$\log(Z/Z_{\odot})^b$	Ref.	F_h^c		
						Model A	Model B	Model C
Cloud head	38.6	−13.1	0 ^d	−0.82 to −0.36	H09	0.153 ± 0.030	0.132 ± 0.017	0.217 ± 0.038
RX J2043.1+0324	49.72	−22.88	14.13	-0.14 ± 0.20	F16	0.449 ± 0.047	0.292 ± 0.043	0.414 ± 0.048
PG 2112+059	57.04	−28.01	22.49	-0.09 ± 0.36	F16	0.493 ± 0.058	0.426 ± 0.066	0.555 ± 0.144
RX J2139.7+0246	58.09	−35.01	27.82	-0.58 ± 0.25	F16	0.535 ± 0.076	0.503 ± 0.085	0.692 ± 0.166

^a Located at $(l, b) = (38^{\circ}67', -13^{\circ}41')$ (L08).

^b SC metallicity, assuming that H09's nitrogen abundance and F16's sulfur abundances correspond directly to the overall metallicity, i.e., $[N/H] = [S/H] = \log(Z/Z_{\odot})$. For the F16 measurements we have combined the statistical and systematic uncertainties.

^c Fraction of high-velocity material along the sight line originating in the halo, extracted from our hydrodynamical models.

^d The tabulated coordinates give the pointing direction of the Wisconsin H α Mapper (WHAM), used by H09. Although this direction is not exactly toward the location of the SC head given in L08, this location lies within the WHAM field of view.

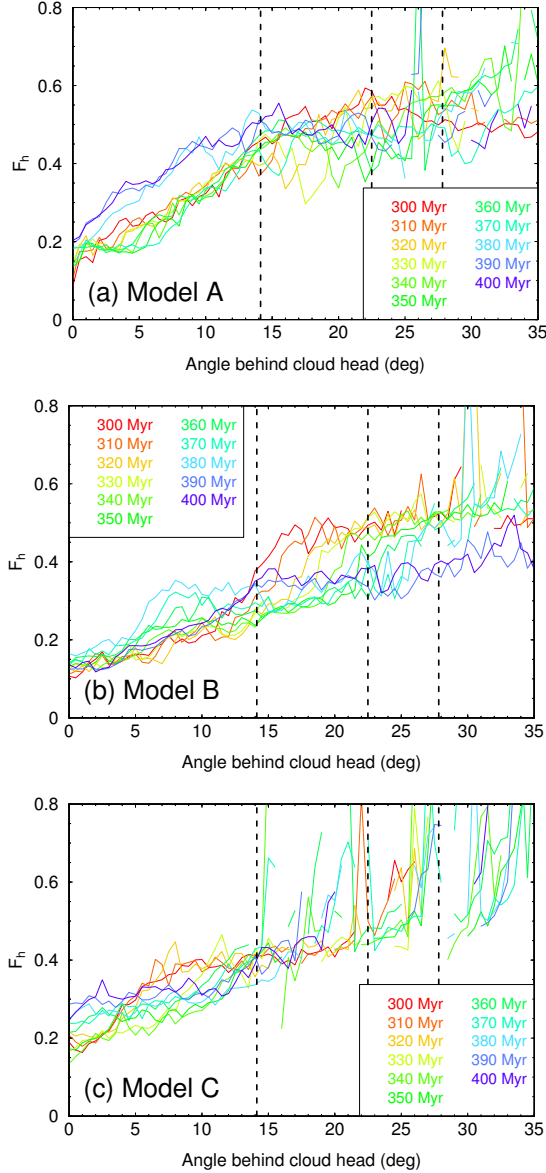


FIG. 5.— The fraction of the high-velocity material originating in the halo, F_h , as a function of angular distance behind the cloud head, extracted from various epochs of Models A–C (top to bottom; see keys). The vertical dashed lines indicate the location of F16’s sight lines relative to the SC head.

Within the epoch-to-epoch variations, these averaged profiles are similar for Models A and B at the cloud head and at angles $\gtrsim 20^\circ$ behind the cloud head. The difference between the models at intermediate angles is because the Model A cloud fragments more than the Model B cloud (as noted above), leading to more rapid mixing in the first few kiloparsecs behind the cloud head. However, other than in the first few kiloparsecs behind the cloud head, the mixing results are not very sensitive to the assumed cooling rate. In contrast, the averaged profiles from Models A and C are similar at all angles, though this is in part due to the large time variation of the Model C profiles. These results suggest that the extent of mixing is not very sensitive to the assumed ambient density.

Figure 7 compares the averaged profiles calculated from versions of our reference model with different

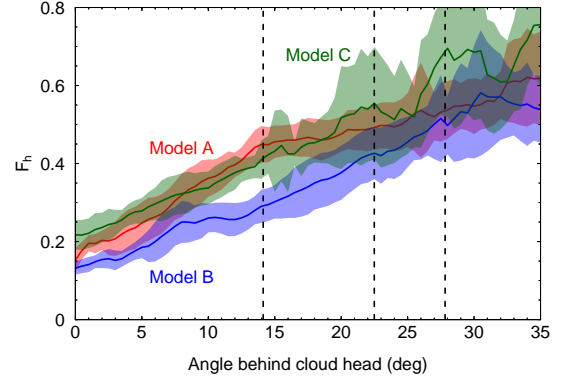


FIG. 6.— F_h sampled every 1 Myr and averaged over $t = 300$ – 400 Myr from Models A, B, and C (red, blue, and green, respectively). The colored bands indicate the standard deviation. The vertical dashed lines indicate the location of F16’s sight lines relative to the SC head.

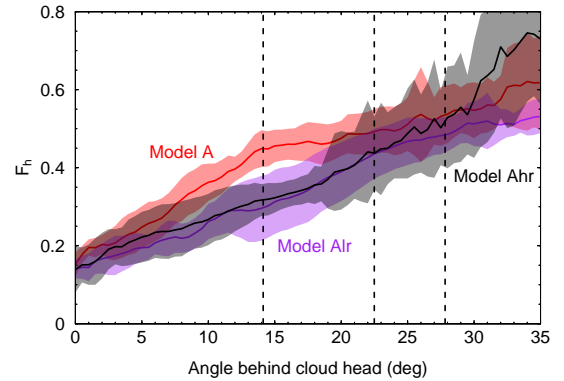


FIG. 7.— Similar to Figure 6, but comparing Models Alr, A, and Ahr, which have maximum resolutions of 20, 10, and 5 pc, respectively (see Table 1).

maximum resolutions. In general, the low- and high-resolution versions of the model (Alr and Ahr, respectively) yield similar results to each other. The standard-resolution version also yields similar results, except for $\sim 7^\circ$ – 19° behind the cloud head. However, when we compare our model predictions with observations in the following section, we find that this discrepancy does not affect our conclusions. We therefore conclude that a maximum resolution of 10 pc (our standard resolution) is adequate for our purposes.

4. COMPARISON WITH OBSERVATIONS

The SC metallicity measurements from H09 and F16 are summarized in Table 2. In addition, we used the values shown in Figure 6 to estimate F_h (the fraction of the high-velocity material that originated in the halo) for synthetic sight lines that cross through the cloud as far behind the SC head and at the same angles as each of the observed sight lines do. These values are shown in the final three columns of Table 2, for each of our three models. The tabulated uncertainties on F_h indicate the one standard deviation variation in the model results.

Figure 8 plots the metallicities observed by H09 and F16 versus the values of F_h we calculated from our models for equivalent lines of sight through the model SC. Overplotted are the metallicities of high-velocity material that would be observed (Z_{obs}) as a function of F_h ,

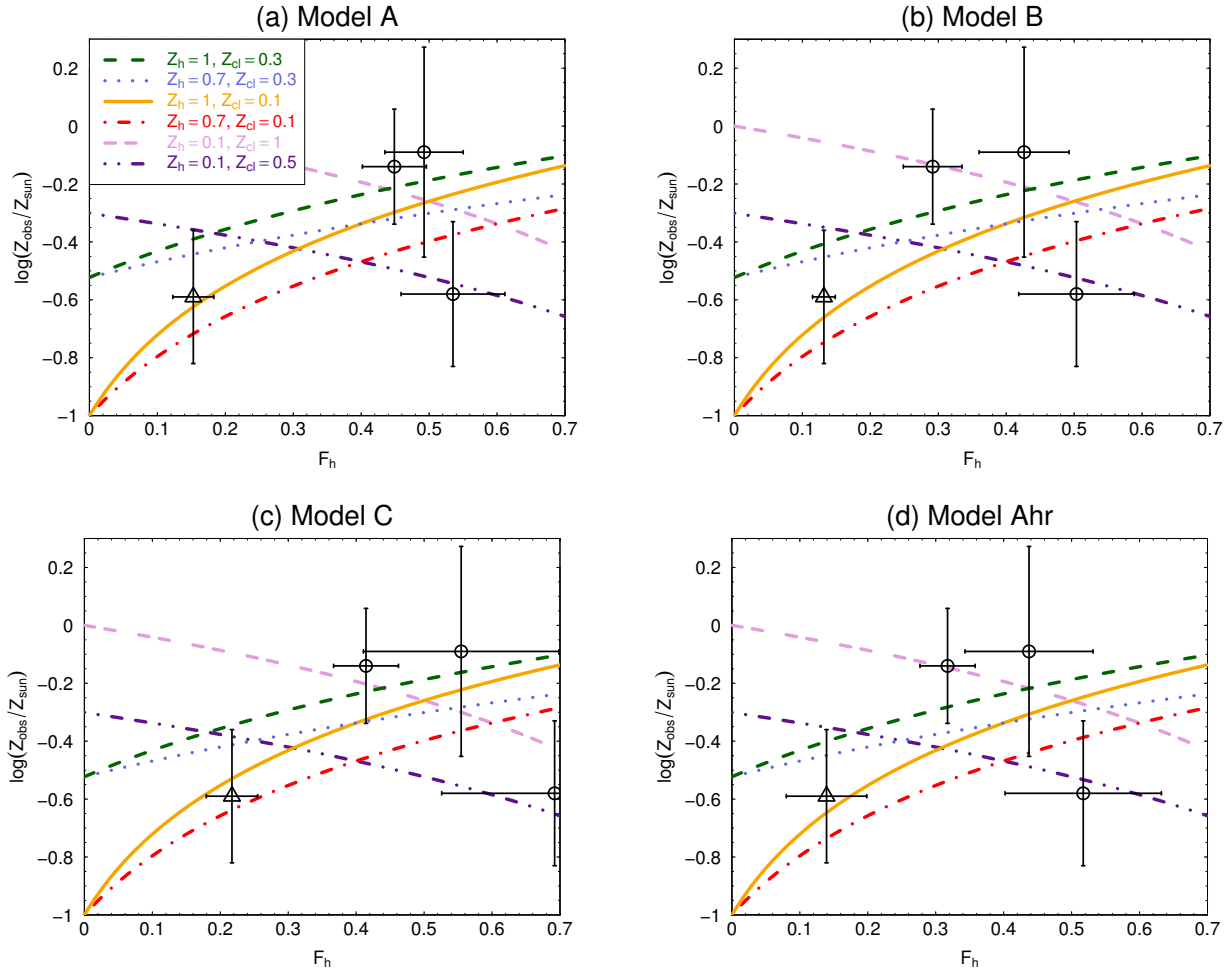


FIG. 8.— Observed SC metallicities (triangle: H09; circles: F16) plotted against the values of F_h that were derived from Models A–C and Ahr ((a)–(d), respectively) for the observed angular separations between the observed directions and the cloud’s head. The error bars indicate 1σ uncertainties. The various curves show the relationships between F_h and the metallicity of high-velocity material that would be expected to be observed for different values of Z_h and Z_{cl} (relative to solar), calculated using Equation (2).

given various possible values of intrinsic halo and cloud metallicities (Z_h and Z_{cl} , respectively) and their relationship

$$Z_{\text{obs}} = F_h Z_h + (1 - F_h) Z_{\text{cl}}. \quad (2)$$

In general, the predictions that assume a metal-rich halo ($Z_h \gtrsim 0.7$) and a metal-poor initial cloud ($Z_{\text{cl}} \lesssim 0.3$) agree with the metallicity measurement for the head and two of the measurements for the tail. However, the metallicity measurement from the sight line furthest down the tail (RX J2139.7+0246, the rightmost data point in Figure 8) is overpredicted. It is possible that the metallicity along the RX J2139.7+0246 sight line is an outlier, as the high-velocity H I column density on this sight line is 4–5 times those on F16’s other two sight lines, despite its being the furthest from the SC head. It is also possible that this sight line passes through a relatively pristine (and therefore low-metallicity, in the scenario considered here) blob of cloud material that was stripped from the head of the cloud without undergoing significant mixing. Such pristine blobs are sometimes seen in the tails of model HVCs (J. A. Gritton, 2016, private communication). Alternatively, the nonmonotonic trend in observed metallicities may indicate spatial vari-

ation in the halo or cloud metallicities. Excluding the RX J2139.7+0246 sight line, the remaining three data points imply $0.1 \lesssim Z_{\text{cl}} \lesssim 0.3$ and $0.7 \lesssim Z_h \lesssim 1.0$. If the halo metallicity is near solar, then $Z_{\text{cl}} \lesssim 0.3$ should be preferred over $Z_{\text{cl}} \sim 0.5$ (the average of the observed metallicities on the four sight lines), as the latter would result in an even higher metallicity along the sight line furthest along the tail.

The predictions in the scenario that assumes a metal-poor halo ($Z_h \sim 0.1$) and a metal-rich initial cloud ($Z_{\text{cl}} \gtrsim 0.5$) also agree with some but not all of the data points. In particular, if the cloud metallicity is large enough to match the measured metallicity on the RX J2043.1+0324 and PG 2112+059 sight lines (the middle two data points in Figure 8), then the metallicity toward the cloud head (the leftmost data point) is overpredicted. However, a metal-poor halo is inconsistent with independent measurements ($Z_h \gtrsim 0.6$; Miller et al. 2016).

Despite the differences between the various models apparent in Figures 6 and 7, the above conclusions are the same for all models (hence our comment in Section 3 that our maximum model resolution of 10 pc appears to be adequate).

5. DISCUSSION AND CONCLUSIONS

Our three-dimensional hydrodynamical simulations of an SC-like cloud passing through halo gas reveal that the tail of the cloud entrains more halo gas than does the head of the cloud. This naturally results in an increase in metallicity from cloud head to tail if the halo has greater metallicity than the cloud (and the reverse if the halo has lesser metallicity than the cloud). The predictions from both scenarios agree with the observed metallicities on some but not all of the observed sight lines; however, the former scenario is preferred as it is in better accord with the findings of Miller et al. (2016) that $Z_h \gtrsim 0.6$.

We explored models with different cooling curves, to represent the uncertainty in the halo and cloud metallicities (our model does not calculate the metallicity dependence of the cooling self-consistently). We also explored models with different ambient densities, representing the change in the ambient density as the SC moves through the halo. While the general conclusions derived from the various models are the same, the differences between the models contribute to the uncertainty in the degree of mixing between the halo and the cloud (as does the time variation within each model). As a result, the uncertainties on the inferred halo and initial cloud metallicities are large.

Our models do not include magnetic fields. Magneto-hydrodynamic (MHD) simulations suggest that magnetic fields suppress mixing between cloud and halo material (McCourt et al. 2015). This suppression of mixing would tend to shift the model predictions in Figure 8 to the left, meaning that the observed metallicity, Z_{obs} , would vary more rapidly with respect to the degree of mixing, F_h . Since, from Equation (2), $dZ_{\text{obs}}/dF_h = Z_h - Z_{\text{cl}}$, this

in turn means that the difference between the halo and initial cloud metallicities inferred from MHD simulations would be larger than from hydrodynamical simulations such as those presented here.

Additional observations could aid in determining the metallicity gradient along the SC. Given the current state of knowledge, we conclude that due to mixing with the halo, the SC's true original metallicity may be less than is implied by H09's and F16's metallicity measurements. Furthermore its uncertainty is likely greater than is implied by the uncertainties on H09's and F16's metallicity measurements. Consequently, the ultimate origin of the SC remains uncertain.

We wish to thank Jason Galyardt for assistance with programming and F. Jay Lockman, Andrew Fox, Alex Hill, J. Chris Howk, and Nicolas Lehner for interesting conversations about the Smith Cloud and other HVCs. We also thank the anonymous referee whose comments helped improve this paper. The software used in this work was developed in part by the DOE NNSA ASC- and DOE Office of Science ASCR-supported Flash Center for Computational Science at the University of Chicago. The simulations were performed at the Georgia Advanced Computing Resource Center (GACRC) of the University of Georgia. We thank Shan-Ho Tsai for her invaluable technical support. We acknowledge use of the R and yt software packages (R Development Core Team 2008; Turk et al. 2011). This research was funded by NASA grant NNX13AJ80G, awarded through the Astrophysics Theory Program.

REFERENCES

- Anders, E., & Grevesse, N. 1989, *Geochim. Cosmochim. Acta*, 53, 197
- Bregman, J. N. 2004, in *Astrophysics and Space Science Library* 312, *High-Velocity Clouds*, ed. H. van Woerden, B. P. Wakker, U. J. Schwarz, & K. S. de Boer (Dordrecht: Kluwer), 341
- Chandrasekhar, S. 1961, *Hydrodynamic and Hydromagnetic Stability* (Oxford: Clarendon Press; Dover reprint, 1981)
- Fox, A. J., Lehner, N., Lockman, F. J., et al. 2016, *ApJL*, 816, L11 (F16)
- Fryxell, B., Olson, K., Ricker, P., et al. 2000, *ApJS*, 131, 273
- Galyardt, J., & Shelton, R. L. 2016, *ApJL*, 816, L18
- Gritton, J. A., Shelton, R. L., & Kwak, K. 2014, *ApJ*, 795, 99
- Henley, D. B., & Shelton, R. L. 2013, *ApJ*, 773, 92
- . 2015, *ApJ*, 808, 22
- Henley, D. B., Shelton, R. L., & Kwak, K. 2014, *ApJ*, 791, 41
- Hill, A. S., Haffner, L. M., & Reynolds, R. J. 2009, *ApJ*, 703, 1832 (H09)
- Kwak, K., Henley, D. B., & Shelton, R. L. 2011, *ApJ*, 739, 30
- Lockman, F. J. 2015, in *Proc. IAU Symp. 315, From Interstellar Clouds to Star-forming Galaxies: Universal Processes?* (Cambridge: Cambridge University Press), in press (arXiv:1511.05423)
- Lockman, F. J., Benjamin, R. A., Heroux, A. J., & Langston, G. I. 2008, *ApJL*, 679, L21 (L08)
- McCourt, M., O'Leary, R. M., Madigan, A.-M., & Quataert, E. 2015, *MNRAS*, 449, 2
- Miller, M. J., & Bregman, J. N. 2013, *ApJ*, 770, 118
- Miller, M. J., Hodges-Kluck, E. J., & Bregman, J. N. 2016, *ApJ*, 818, 112
- Nichols, M., Mirabal, N., Agertz, O., Lockman, F. J., & Bland-Hawthorn, J. 2014, *MNRAS*, 442, 2883
- Putman, M. E., Peek, J. E. G., & Jounge, M. R. 2012, *ARA&A*, 50, 491
- R Development Core Team. 2008, *R: A Language and Environment for Statistical Computing* (Vienna, Austria: R Foundation for Statistical Computing)
- Smith, G. P. 1963, *Bull. Astron. Inst. Netherlands*, 17, 203
- Sutherland, R. S., & Dopita, M. A. 1993, *ApJS*, 88, 253
- Turk, M. J., Smith, B. D., Oishi, J. S., et al. 2011, *ApJS*, 192, 9
- Wakker, B. P., & van Woerden, H. 1997, *ARA&A*, 35, 217
- Wolfire, M. G., Hollenbach, D., McKee, C. F., Tielens, A. G. G. M., & Bakes, E. L. O. 1995a, *ApJ*, 443, 152
- Wolfire, M. G., McKee, C. F., Hollenbach, D., & Tielens, A. G. G. M. 1995b, *ApJ*, 453, 673